

A Novel Intergrowth Structure Between ReO_3 -Type and Tetragonal Tungsten Bronze-Type in the Zr/Nb/W/O System

FRANK KRUMEICH,*† GEORG LIEDTKE AND WERNER MADER

Institut für Anorganische Chemie der Universität Bonn, Römerstrasse 164, D-53117 Bonn, Germany. E-mail: fmk@aca.fta-berlin.de

(Received 6 March 1996; accepted 24 May 1996)

Abstract

The intergrowth structure of a zirconium niobium tungsten oxide has been determined by transmission electron microscopy methods. Electron diffraction patterns reveal the parameters of the monoclinic lattice: $a = 19.0$, $b = 3.9$ and $c = 13.8$ Å; $\beta = 93.5^\circ$. Additional reflections in higher-order Laue zones indicate the presence of a diagonal glide plane, leading to a larger unit cell. A structure model of composition $\text{Zr}_n\text{Nb}_{8-2n}\text{W}_{12+n}\text{O}_{56}$ ($0.5 < n < 1$) has been derived from high-resolution lattice images. Alternating slabs of ReO_3 -type and of tetragonal tungsten bronze structure are intergrown coherently. Two five-membered rings of MO_6 octahedra belonging to adjacent tetragonal tungsten bronze subcells are connected by having two octahedra in common. For the first time, this arrangement of double pentagons is observed in a regular structure.

1. Introduction

Ordered intergrowth between ReO_3 - and TTB-type (tetragonal tungsten bronze) structures is a common feature (Marinder, 1986) in the tungsten-rich part of the system $\text{Nb}_2\text{O}_5/\text{WO}_3$. The structure of the 2:7 phase ($2\text{Nb}_2\text{O}_5 \times 7\text{WO}_3$) consists of square arrays of ReO_3 -type ($4 \times 4 \times \infty$ blocks of corner-sharing MO_6 octahedra; $M = \text{Nb}, \text{W}$) embedded into the TTB matrix (Iijima & Allpress, 1974). A different type of intergrowth is present in the structures of the 4:22 and 4:50 phases, in which slabs of ReO_3 structure and single TTB units occur alternately (Iijima, 1978). Furthermore, $\text{W}_{24}\text{O}_{68}$ (Sundberg, 1978/1979) crystallizes in a similar structure (Fig. 1). The different widths of the ReO_3 slabs typify these three structures, e.g. in $\text{W}_{24}\text{O}_{68}$, the slab is only a single WO_6 octahedron wide. The structures of these intergrowth phases were derived from HRTEM (high-resolution transmission electron microscopy) images.

Starting with $\text{Nb}_8\text{W}_9\text{O}_{47}$ [4:9 phase (Sleight, 1966)], solid-solution series $\text{Nb}_{8-n}\text{W}_{9+n}\text{O}_{47}$ ($0 \leq n \leq 5$) were obtained by systematic substitution of Nb^{5+} by Nb^{4+}

or W^{4+} , respectively, and W^{6+} according to $2\text{Nb}^{5+} \equiv \text{M}^{4+} + \text{W}^{6+}$. The threefold TTB superstructure of the 4:9 phase is preserved by this (Krumeich, Hussain, Bartsch & Gruehn, 1995). Moreover, it is possible to incorporate other tetravalent cations such as Zr^{4+} in this structure (Krumeich, Liedtke & Mader, 1995). Indeed the X-ray powder diffraction pattern of $\text{ZrNb}_6\text{W}_{10}\text{O}_{47}$ exhibits the reflections of a 4:9-type structure. Complementary TEM investigations confirmed that most crystallites belong to the 4:9-type phase. Additionally, several crystal fragments have been found belonging to a novel type of intergrowth structure. The determination of its approximate structure by TEM methods is reported in the present study.

2. Experimental

ZrO_2 (Merck), Nb_2O_5 (Fluka) and WO_3 (Fluka) were mixed in the mole ratio 1:3:10, giving the composition $\text{ZrNb}_6\text{W}_{10}\text{O}_{47}$. The mixture was annealed in air (1473 K, 3 d) in a sealed platinum ampoule. The microcrystalline product was characterized by X-ray powder diffraction

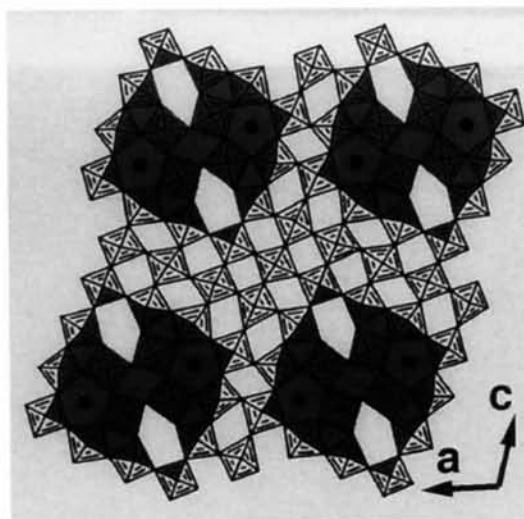


Fig. 1. Crystal structure of $\text{W}_{24}\text{O}_{68}$ in projection along [010] (Sundberg, 1978/1979). TTB-type subcells are shaded with empty pentagonal tunnels left open.

† Present address: Institut für Angewandte Chemie Berlin–Adlershof, Rudower Chaussee 5, D-12484 Berlin, Germany

(Guinier method) and TEM methods (Krumeich, Liedtke & Mader, 1995).

For electron microscopy the product was ground in an agate mortar and suspended in acetone. Some droplets were brought onto a perforated foil (carbon-coated Formvar) supported by a copper grid. TEM investigations were performed on a Philips CM30ST microscope operated at 300 kV. Using a double tilt holder, thin crystal flakes were orientated to be observed in the direction of the short crystallographic b axis. The lattice images were recorded near the Scherzer focus so that the cation sites are visible as dark dots (Horiuchi, Muramatsu & Matsui, 1978). This correspondence has been verified by image simulations (Krumeich, Hussain, Bartsch & Gruhn, 1995) using the multi-slice method [EMS program (Stadelmann, 1987)]. The cation ratios of the investigated crystals were determined by quantitative EDX (energy-dispersive X-ray) analyses (Tracor Voyager system, Ge detector). In order to obtain the most accurate results, the Nb/W ratio was calibrated with $\text{Nb}_8\text{W}_9\text{O}_{47}$ used as a standard.

3. Results

The new intergrowth phase has been detected and characterized by TEM methods. No indication of this structure has been found by X-ray powder diffraction. In the electron diffraction patterns (along [010], Fig. 2a) the strongest reflections, arranged in a square, correspond to a ReO_3 -type substructure. Their distances are measured to give a d spacing of $\sim 3.8 \text{ \AA}$. The superstructure reflections indicate a monoclinic unit cell that is metrically related to the ReO_3 -type subcell. 17 superstructure reflections are located between the main spots in the $[30\bar{2}]^*$ as well as in the $[304]^*$ direction of the ReO_3 -type sublattice. Therefore, the reciprocal lattice parameters can be deduced with reference to those of the subcell

$$\bar{a}^* = 1/18[30\bar{2}]_{\text{ReO}_3}^*, \bar{c}^* = 1/18[304]_{\text{ReO}_3}^*, \beta^* = 86.5^\circ.$$

The length of the b axis is obtained from the diameter of the FOLZ (first-order Laue zone) ring in a CBED (convergent beam electron diffraction) pattern taken

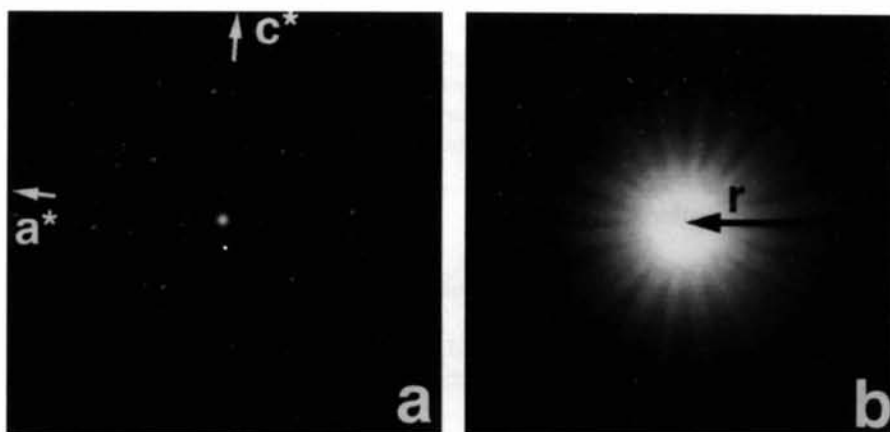


Fig. 2. (a) Electron diffraction and (b) CBED pattern along [010], $r = 0.39 \text{ nm}^{-1}$.



Fig. 3. HRTEM image along [010] showing a perfectly ordered crystal region.

along [010] (Fig. 2b). The resulting unit-cell dimensions are

$$\tilde{a} = 19.0, \tilde{b} = 3.9 \text{ and } \tilde{c} = 13.8 \text{ \AA}; \tilde{\beta} = 93.5^\circ.$$

The length of the short crystallographic axis corresponds to the diagonal in a MO_6 octahedron. Hence, it follows that the polyhedra arrangement in the ac plane determines the structural features, whereas their connection by corner-sharing leads to polyhedra columns along the b axis. The cation sites are detectable by HRTEM so that essential structural information is provided by micrographs taken from thin crystal regions along [010] (Fig. 3). The cation sites located in the centers of the

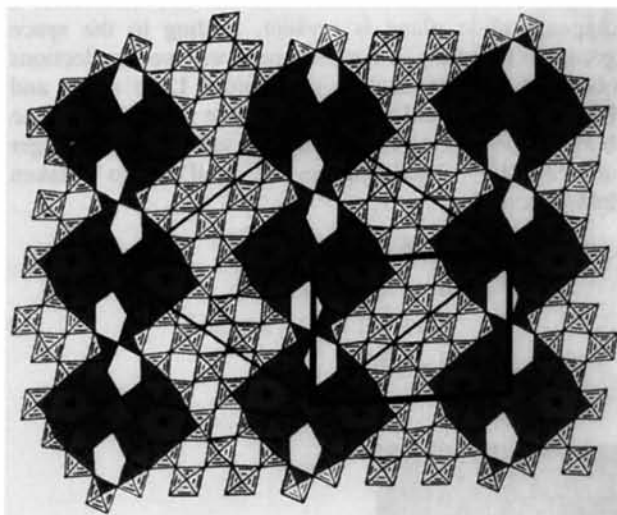


Fig. 4. Structural model of $Zr_n Nb_{8-2n} W_{12+n} O_{56}$ in projection along [010]. TTB-type subcells are shaded with empty pentagonal tunnels left white. The small and large unit cells are outlined.

Table 1. Fractional atomic coordinates of metal atoms ($M = Zr, Nb, W$)

Space group Pm , $Z = 1$; $a = 19.0, b = 3.9, c = 13.8 \text{ \AA}; \beta = 93.5^\circ$.

	x	y	z
M1	0.08	0.5	0.854
M2	0.224	0.5	0.96
M3	0.075	0.5	0.571
M4	0.103	0.5	0.127
M5	0.175	0.5	0.365
M6	0.238	0.5	0.714
M7	0.391	0.5	0.913
M8	0.333	0.5	0.508
M9	0.293	0.5	0.167
M10	0.471	0.5	0.317
M11	0.498	0.5	0.699
M12	0.655	0.5	0.857
M13	0.626	0.5	0.495
M14	0.575	0.5	0.087
M15	0.77	0.5	0.056
M16	0.736	0.5	0.294
M17	0.925	0.5	0.167
M18	0.902	0.5	0.429
M19	0.779	0.5	0.635
M20	0.891	0.5	0.889

polyhedra are recognizable as dark dots so that their positions in projection onto the ac plane are extractable from the lattice images (Table 1). All metal atoms are assumed to be located in a plane together with the O atoms laying between them (atomic sites: $x, \frac{1}{2}, z$). The oxygen positions are not visible in the lattice images; reasonable positions have been estimated. The coordination spheres of the cations are completed by more O atoms localized in the midst between the cations in the direction of the b axis. Because of these assumptions concerning the crystal symmetry, a mirror plane perpendicular to [010] appears. Therefore, the space group Pm [number 6 (Hahn, 1989)] is chosen for the derivation of the

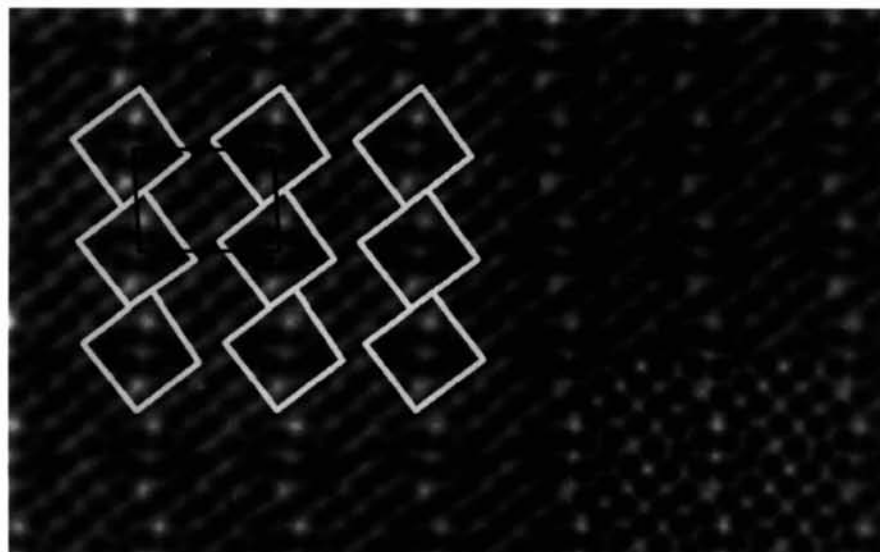


Fig. 5. HRTEM image with slabs of TTB-type subcells and a unit cell outlined. The inset (lower right side) shows the simulated image (parameters: $C_s = 1.2 \text{ mm}$, $U = 300 \text{ kV}$, thickness $d = 7.8 \text{ nm}$, defocus $\epsilon = -30 \text{ nm}$).

structural model (Fig. 4). The structural parameters and approximate cation positions are listed in Table 1.

The correspondence between the structural model and HRTEM image can be observed directly in the

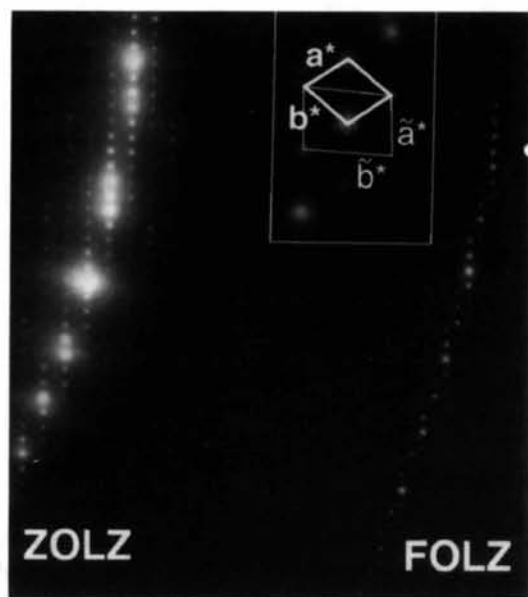


Fig. 6. Electron diffraction pattern of a tilted crystal; in the center of the reciprocal unit cell (inset), an additional reflection is present in the higher-order Laue zone.

enlarged crystal region shown in Fig. 5. Parallel slabs of ReO_3^- and TTB-type structures (outlined) occur perfectly ordered. Very bright dots in the lattice image correspond to the empty pentagonal tunnels in the TTB units. Furthermore, image simulations have been calculated with the derived structural data (Table 1) and the experimental parameters of the electron microscope. The excellent match between calculated (inset in Fig. 5) and experimental image supports the structural model.

In order to obtain information in the direction of the b axis, tilting experiments have been performed to reveal the full reciprocal lattice. A diffraction pattern obtained by tilting the crystal out of b^* by $\sim 10^\circ$ is shown in Fig. 6, where the FOLZ contains reflections of the type $(h/2, 1, l/2)$ in the old notation. The corresponding reflection condition is $h + l = 2n$ for $h0l$. Therefore, a diagonal glide plane is present, leading to the space group Pn (number 7). Furthermore, very weak reflections observed between ZOLZ (zero-order Laue zone) and FOLZ (of the small unit cell) indicate a doubling of the b axis. Considering this additional information, a larger unit cell (3D – three-dimensional – cell) has to be taken into account

$$\mathbf{a} = \tilde{\mathbf{a}} + \tilde{\mathbf{b}}, |\mathbf{a}| = 21.6 \text{ \AA};$$

$$\mathbf{b} = 2\tilde{\mathbf{b}}, |\mathbf{b}| = 7.8 \text{ \AA};$$

$$\mathbf{c} = -\tilde{\mathbf{a}} + \tilde{\mathbf{b}}, |\mathbf{c}| = 23.0 \text{ \AA};$$

$$\beta = 108^\circ.$$

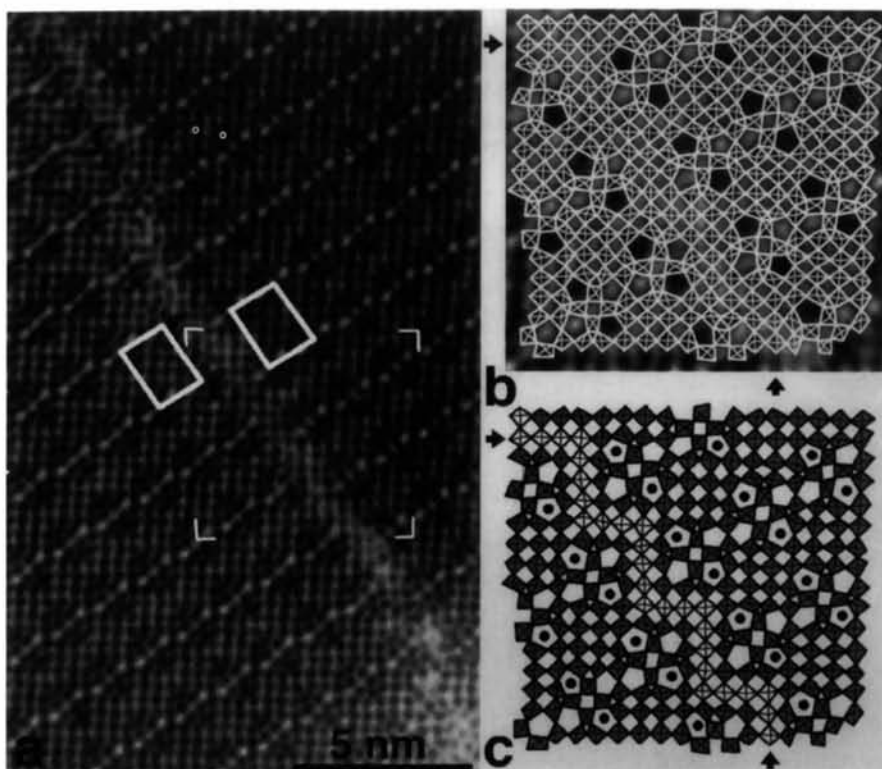


Fig. 7. (a) HRTEM image of a planar defect, the displacement is visualized by the shift of the unit cells (outlined); (b) enlargement with structural model superimposed; (c) structural model; the additional slab of octahedra (white) is indicated by arrows (in b and c).

Since the HRTEM investigations provide no information on the origin of these superstructures, only the structure of the smaller cell (2D cell) is used in the following for discussion of the structure and defects.

The crystals exhibiting this new structure are almost perfectly ordered (Fig. 3), only a few defects have been observed. A displacement (along [100]), present in the crystal area shown in Fig. 7(a), is clearly recognizable by the shift in rows of bright dots. The fault boundary exhibits an ordered structure in its central area. An enlargement is shown in Fig. 7(b) with the octahedral arrangement superimposed on the HRTEM image. Again, dark contrasts correspond to the cation sites. The displacement is caused by an additional slab of octahedra (Fig. 7c) located between the TTB-type subunits of the intergrowth structure. This arrangement is similar to the structure of $W_{24}O_{68}$ (Fig. 1), but the connection of the TTB units is different. In the upper part of Fig. 7(a), the defect boundary is shifted along [001].

4. Discussion

The closely related structures of TTB- and ReO_3 -types both consist of corner-sharing MO_6 octahedra. In the ReO_3 -type structure the octahedra occupy the positions of a primitive cubic lattice so that square tunnels appear running along the axes. In the TTB structure, trigonal and pentagonal tunnels occur along [001] besides square ones. Furthermore, a geometrical relationship exists: A 4×4 block of octahedra (ReO_3 -type) can be modified by a 45° rotation of its four central octahedra resulting in the unit cell of the TTB-type (Hyde & O'Keeffe, 1973). Therefore, intimate intergrowth of TTB- and ReO_3 -type structures is a favored feature in systems in which both structures occur. The structures of $W_{24}O_{68}$ (Fig. 1) as well as niobium tungsten oxides (4:22 and 4:50 phases) consist of parallel slabs of ReO_3 - and TTB-type subcells. Five-membered rings of octahedra (pentagons) are connected *via* a square array of octahedra in between them [diamond link (Lundberg, Sundberg & Magnéli, 1982)]. Adjacent TTB subcells are joined in this way. The corresponding pentagonal tunnels are filled with metal–oxygen strings leading to the so-called pentagonal columns (Marinder, 1986). A completely different type of connection combines the TTB units in the new phase (Fig. 4): Pentagons belonging to adjacent TTB subcells are linked directly by edge-sharing. Their pentagonal tunnels are empty. The pentagons have two octahedra in common so that a double pentagon results. This is a rather unusual structural element which had been observed before only in defects of tungsten-rich $(Nb,W)O_{2.925}$ (England & Tilley, 1982) and in oxidation products of $W_{18}O_{49}$ (Sahle, 1982, 1983) and $Nb_4W_{13}O_{47}$ (Krumeich, Bartsch & Gruehn, 1995). The principle of their arrangement is similar in $(Nb,W)O_{2.925}$ and the new phase (Fig. 5): Double pentagons form chains in which they are connected *via* squares of octahedra (diamond

link). These squares are located in the center of TTB-type subcells, in which two of the four pentagonal tunnels are involved in the chain, whereas the others are filled with metal–oxygen strings. In the new structure the ReO_3 - and TTB-type subcells are stacked alternating with each other in the [101] direction (Fig. 5). Both subcells are close to being squares of $12.2 \times 12.2 \text{ \AA}^2$, so that a perfect fit results.

Provided that the cations have either an octahedral (CN = 6) or a pentagonal bipyramidal (CN = 7) oxygen coordination, the general formula of the suggested unit cell is $M_{20}O_{56}$. This formula may apply to a hypothetical niobium tungsten oxide $Nb_8W_{12}O_{56}$, which would be the end member ($n = 0$) of a solid solution series $Zr_nNb_{8-2n}W_{12+n}O_{56}$. The EDX analyses show the presence of zirconium in the investigated crystals; their compositions correspond to $n \simeq 0.5 - 1$. Since Zr^{4+} prefers a coordination higher than 6, *e.g.* in ZrO_2 , it is likely to be located in the pentagonal bipyramidal sites rather than in the octahedral ones.

The presence of a diagonal glide plane is caused either by a systematic displacement (along *b*) of cations out of the position on the mirror plane ($y = 0.5$) in the suggested structure model (Fig. 4) or an alternate stacking (along *b*) of different cations in one or more positions. The last possibility seems to be more reasonable, since it explains the observed doubling of the *b* axis. Since there is no chance to reveal the structural reason for the glide plane by TEM methods, only X-ray investigations of single crystals would help to solve this problem. Attempts to prepare $ZrNb_6W_{13}O_{56}$ as a pure phase by heating mixtures of the binary oxides in the corresponding mole ratio have failed up to now.

Considering the almost perfect order in the observed crystal regions of the new phase (Fig. 3), one can conclude that the incorporation of zirconium stabilizes a structure which, apparently, does not exist in the pseudo-binary Nb_2O_5/WO_3 system.

Financial support of G. Liedtke by the Ministerium für Wissenschaft und Forschung NRW is gratefully acknowledged.

References

- England, P. J. & Tilley, R. J. D. (1982). *Chem. Scr.* **20**, 102–107.
- Hahn, T. (1989). *International Tables for Crystallography*, Vol. A. Dordrecht: Kluwer Academic Publishers.
- Horiuchi, S., Muramatsu, K. & Matsui, Y. (1978). *Acta Cryst.* **A34**, 939–946.
- Hyde, B. G. & O'Keeffe, M. O. (1973). *Acta Cryst.* **A29**, 243–248.
- Iijima, S. (1978). *Acta Cryst.* **A34**, 922–931.
- Iijima, S. & Allpress, J. G. (1974). *Acta Cryst.* **A30**, 22–29.
- Krumeich, F., Bartsch, C. & Gruehn, R. (1995). *J. Solid State Chem.* **120**, 268–274.
- Krumeich, F., Hussain, A., Bartsch, C. & Gruehn, R. (1995). *Z. Anorg. Allg. Chem.* **621**, 799–806.

- Krumeich, F., Liedtke, G. & Mader, W. (1995). *Optik*, **100**, Suppl. 6, 62.
- Lundberg, M., Sundberg, M. & Magnéli, M. (1982). *J. Solid State Chem.* **44**, 32–40.
- Marinder, B.-O. (1986). *Angew. Chem. Int. Ed. Engl.* **25**, 431–442.
- Sahle, W. (1982). *J. Solid State Chem.* **45**, 334–342.
- Sahle, W. (1983). *Chem. Commun. Univ. Stockholm*, **4**, 42–46.
- Sleight, A. W. (1966). *Acta Chem. Scand.* **20**, 1102–1112.
- Stadelmann, P. (1987). *Ultramicroscopy*, **21**, 131–146.
- Sundberg, M. (1978/1979). *Chem. Scr.* **14**, 161–166.